# Direct Probing of the Phosphate-Ion Distribution in Bioactive Silicate Glasses by Solid-State NMR: Evidence for Transitions between Random/Clustered Scenarios

Renny Mathew,[†] Claudia Turdean-Ionescu,[†] Baltzar Stevensson,[†] Isabel Izquierdo-Barba,[‡,§] Ana García,[‡,§] Daniel Arcos,[‡,§] María Vallet-Regí,[‡,§] and Mattias Edén*,[†]

[†]Physical Chemistry Division, Department of Materials and Environmental Chemistry, Arrhenius Laboratory, Stockholm University, SE-106 91, Stockholm, Sweden

[‡]Departamento de Química Inorgánica y Bioinorgánica, Facultad de Farmacia, Universidad Complutense de Madrid, 28040 Madrid, Spain

[§]Networking Research Center on Bioengineering, Biomaterials and Nanomedicine (CIBER-BBN), Madrid, Spain

Ⓢ *Supporting Information*

ABSTRACT: By employing ^{31}P multiple-quantum coherence-based solid-state nuclear magnetic resonance spectroscopy, we present the first comprehensive experimental assessment of the nature of the orthophosphate-ion distributions in silicate-based bioactive glasses (BGs). Results are provided both from melt-prepared BG and evaporation-induced self-assembly-derived mesoporous bioactive glass (MBG) structures of distinct compositions. The phosphate species are randomly dispersed in melt-derived BGs (comprising 44−55 mol % SiO_2) of the $Na_2O−CaO−SiO_2−P_2O_5$ system, whereas a Si-rich (86 mol % SiO_2) and Ca-poor ordered MBG structure exhibits nanometer-sized amorphous calcium phosphate clusters, conservatively estimated to comprise at least nine orthophosphate groups. A Ca-richer MBG (58 mol % SiO_2) reveals a less pronounced phosphate clustering. We rationalize the variable structural role of P in these amorphous biomaterials.

KEYWORDS: bioactive glasses, phosphate distribution, calcium phosphate clusters, multiple-quantum coherence, 45S5 Bioglass
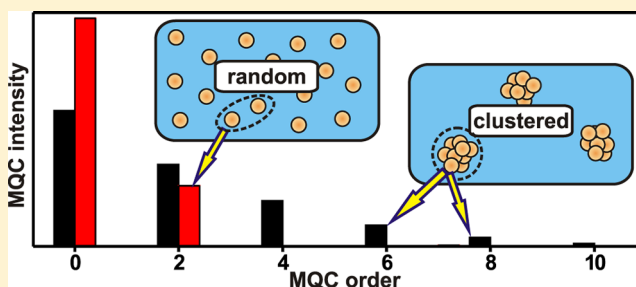
1. INTRODUCTION

Bioactive silicophosphate glasses (BGs) are widely exploited as grafting materials in periodontal and orthopedic surgery.[1−3] On contact with body fluids, they integrate with human tissues by forming a biomimetic calcium hydroxy-carbonate apatite (HCA) surface-layer.[1−10] Melt-prepared BGs of the $Na_2O−CaO−SiO_2−P_2O_5$ system, such as the extensively investigated and clinically utilized "45S5" Bioglass,[1−3,11,12] only exhibit bone-bonding ability, henceforth referred to as "bioactivity", over fairly narrow compositional ranges (∼35−55 mol % SiO_2).[3] They require large amounts of Na^+/Ca^{2+} glass modifiers for ensuring sufficiently fragmented networks to readily degrade in vitro/vivo.[7−10] Owing primarily to their enhanced surface-areas, sol−gel or evaporation-induced self-assembly[4,13] (EISA) processes may provide silica-richer BGs that feature excellent bioactivities;[3,4,14−26] the surface features lower-connectivity silanol [$SiO_3(OH)$] moieties, whose presence partially relaxes the need for modifier-rich compositions.[3,4,17,22,23] This particularly concerns Ca-bearing EISA-generated *mesoporous bioactive glasses* (MBGs) that exhibit ordered mesoporous networks and amorphous SiO_2-based pore-walls.[4,18−20]

All (M)BG structures involve a network of interconnected SiO_4 tetrahedra, whereas P predominantly exists as orthophosphate ions that are charge-balanced by the glass modifier cations (e.g., Na^+ and Ca^{2+}).[3,8−12,21−23,27,28] The remainder of the modifier reservoir depolymerizes the glass network by breaking Si−O−Si linkages and introducing nonbridging oxygen (NBO) ions that associate with the glass modifier cations.[3,8−12,21−23,27,28] The bioactivity of a melt-prepared BG depends primarily on its P content[5−10] and silicate-network connectivity,[7−10] i.e., the average number of bridging oxygen (BO) atoms per SiO_4 moiety (N_{BO}). Regardless of the BG-preparation method, the in vitro/vivo HCA-formation rate at the (M)BG surface is known to accelerate as the P_2O_5 content increases up to a few mol %.[5,6,8−10] This trend is observed as long as the phosphate speciation remains as readily released *ortho*phosphate groups,[10,29,30] as opposed to covalently linked P−O−P or P−O−Si moieties, whose presence in P-rich and modifier-poor glasses accounts for the transition to bio*inactive* compositions.[29,30]

Table 1. (M)BG Sample Compositions[a]

| | oxide equivalent | | | | | | | | stoichiometric formula[b] | N_{BO}[c] | ρ (gcm^{-3})[d] |
| | nominal | | | | analyzed | | | | | | |
sample	Na$_2$O	CaO	SiO$_2$	P$_2$O$_5$	Na$_2$O	CaO	SiO$_2$	P$_2$O$_5$			
MBG86(3.4)	–	0.100	0.850	0.050	–	0.105	0.861	0.034	Ca$_{0.098}$Si$_{0.838}$P$_{0.064}$O$_{1.934}$	4.00	2.28
MBG58(4.3)	–	0.370	0.580	0.050	–	0.380	0.577	0.043	Ca$_{0.364}$Si$_{0.554}$P$_{0.082}$O$_{1.676}$	3.13	2.58
BG44(6.0)	0.219	0.287	0.434	0.060	0.201	0.274	0.460	0.065	Na$_{0.343}$Ca$_{0.223}$Si$_{0.340}$P$_{0.094}$O$_{1.310}$	2.50	2.71
BG48(4.0)	0.209	0.271	0.480	0.040	0.193	0.254	0.509	0.044	Na$_{0.334}$Ca$_{0.217}$Si$_{0.385}$P$_{0.064}$O$_{1.314}$	2.50	2.69
BG55(4.0)	0.179	0.233	0.548	0.040	0.162	0.226	0.572	0.040	Na$_{0.294}$Ca$_{0.191}$Si$_{0.449}$P$_{0.066}$O$_{1.401}$	2.93	2.64
BG46(2.6)	0.244	0.269	0.461	0.026	0.229	0.255	0.486	0.030	Na$_{0.384}$Ca$_{0.212}$Si$_{0.363}$P$_{0.041}$O$_{1.233}$	2.11	2.70

[a]Comparison between the batched and analyzed compositions (utilizing XRF for the MBGs and SEM/EDX for the BGs). [b]The stoichiometric formula is based on the analyzed (for MBGs) and nominal (for BGs) compositions. [c]The average number of bridging oxygen atoms per SiO$_4$ tetrahedron, obtained after accounting for the modifier cation-consumption of the orthophosphate species in each sample, as described in detail in refs 10 and 23. Note that for the MBGs, this calculation is only representative for the pore-wall interior, as it ignores the lower-connectivity SiO$_3$(OH) groups at the MBG surface; see Gunawidjaja et al.[22,23] for further discussions. [d]Densities (within ±0.005 gcm^{-3}) were determined by the Archimedes method in water at 22 °C, except for those of the MBG pore-walls, whose skeletal densities were measured by a AccuPyc 1330 helium pycnometer.

Characterizing the distribution of a minor chemical species (such as orthophosphate ions) in an amorphous matrix over a nanometer scale is a commonly encountered but extremely challenging problem, where traditional diffraction and electron microscopy techniques may normally not provide detailed information. Indeed, whereas it is well acknowledged that the (M)BG bioactivity strongly depends on the P-content, little is known about the spatial distribution of the orthophosphate ions across the structure, and statements in the literature[3,8,9] are vague and/or contradictory.

In the case of CaO−SiO$_2$−P$_2$O$_5$ MBGs, our recent work has resulted in a proposed pore-wall constitution that involves a main silica-rich CaO−SiO$_2$ component, interleaved by (presumably) nanometer-sized and surface-associated amorphous calcium orthophosphate (CaP) clusters.[21] While built around circumstantial evidence from ^{29}Si/^{31}P solid-state nuclear magnetic resonance (NMR),[21,22] and commensurate with inferences from transmission electron microscopy (TEM) about a uniform cation-dispersion over tens of nanometers,[18−20] this MBG pore-wall model awaits *direct* experimental proof. Also for melt and sol−gel derived BGs, several groups have recently suggested the presence of either analogous nanocrystalline CaP clusters[31,32] or "glass-in-glass" separation into Si- and P-rich phases.[8,9] However, these conclusions are often drawn from TEM/electron diffraction data on individual sample fragments, and it is unclear how well they represent the total P speciation.

In this work, we shed light on the potential (non)clustering of the orthophosphate ions by its direct experimental probing across the entire structures of BGs prepared by either melt-quench or EISA procedures and featuring variable compositions. The homonuclear through-space ^{31}P−^{31}P dipolar interaction in solid-state NMR spectroscopy offers a route to gain insight into the spatial distribution of orthophosphate species across a structure. The interaction-strength in a spin-pair (j−k) is reflected by the dipolar coupling constant (b_{jk}) that displays an inverse cubic dependence on the ^{31}P−^{31}P internuclear distance r_{jk}. Dipolar-coupling-based solid-state NMR techniques may be exploited to assess the number M of spatially proximate spin-1/2 nuclei (such as ^{31}P) via the successful excitation of the Mth order multiple-quantum coherence (MQC).[33−36] By applying a radio frequency (rf) pulse sequence that generates a double-quantum (2Q) effective Hamiltonian to the spin ensemble at thermal equilibrium, all *even MQC* orders (M = 2, 4, 6,...) progressively develop as the excitation interval (τ_{exc}) grows.[33−36]

Herein, we employ such ^{31}P "spin-counting" techniques, complemented by quantitative results from selective 2QC excitation NMR experiments under magic-angle spinning (MAS) conditions, for characterizing the P distributions in a series of (M)BG structures, which is observed to vary depending on the silica content and preparation route of the BG: melt-derived BGs exhibit randomly dispersed orthophosphate groups, whereas EISA-generated MBGs manifest pronounced CaP clustering. During the writing of this paper, Fayon et al.[37] reported ^{31}P spin-counting results from one melt-derived CaO−SiO$_2$−P$_2$O$_5$ glass exhibiting identical Si and P contents as our BG46(2.6) specimen, i.e., "45S5" Bioglass.[1] By the availability of a larger set of samples and data in the present study leads us to draw somewhat different conclusions regarding the nature of the phosphate distribution in BGs.

We examine two distinct CaO−SiO$_2$−P$_2$O$_5$ MBG specimens [MBG86(3.4); MBG58(4.3)], as well as four melt-prepared Na$_2$O−CaO−SiO$_2$−P$_2$O$_5$ glasses [BG46(2.6); BG48(4.0); BG55(4.0); BG44(6.0)], where (M)BGn(p) implies n and p mol % of SiO$_2$ and P$_2$O$_5$, respectively. Table 1 lists the sample compositions. Both the BG48(4.0) and BG44(6.0) samples exhibit N_{BO} = 2.50. To explore the potential influences from the silicate-network connectivity on the PO$_4^{3-}$ distribution, we also provide results from a SiO$_2$-richer BG55(4.0) specimen featuring N_{BO} = 2.93 for comparison with its BG48(4.0) counterpart. BG46(2.6) corresponds to the "45S5" composition,[1] associated with N_{BO} = 2.11.

2. MATERIALS AND METHODS

2.1. Sample Preparations and Characterization. Crystalline calcium hydroxyapatite (HAp; Ca$_5$(PO$_4$)$_3$OH) was used as received from Aldrich (99.99% purity). The remaining (M)BG samples were prepared and characterized as described below.

2.1.1. Melt-Prepared Glasses. The BGn(p) specimens were prepared in batches of 6.0 g by the standard melt-quench method, using precursors of NaH$_2$PO$_4$ (99.99%; Merck) and Na$_2$CO$_3$ (99.9%), CaCO$_3$ (99.9%), SiO$_2$ (99.99%) from ChemPur. The batched glass compositions are listed in Table 1, with the mass of each component calculated to provide the desired composition in oxide equivalents and accounting for the mass-loss of CO$_2$ stemming from the carbonate decomposition during heating. A 0.1 wt % amount of Fe$_2$O$_3$ was added to each batch to accelerate spin−lattice relaxation for the NMR experimentation. This had otherwise no significant bearing on the results. Each precursor-mixture was ball-milled for 12 h, subsequently placed in a Pt crucible, and heated in an electric furnace at 950 °C for 4 h

to ensure complete carbonate decomposition. The temperature was then increased to 1350 °C [for BG46(2.6)], 1550 °C [for BG48(4.0) and BG44(6.0)], or 1620 °C [for BG55(4.0)], where each melt was held for 4 h prior to quenching by immersing the bottom of the crucible in water. The evaporation losses during synthesis were typically ≲ 1.5 wt %.

Each sample was examined by powder X-ray diffraction (XRD), by using a PANalytical X'pert PRO MPD diffractometer and Cu $K\alpha_1$ radiation. The data collection lasted for 4 h per sample, with 2θ ranging between 10° and 70°. No crystalline phases were observed within an estimated lower detection limit of ≲ 1%.

Surface-polished glasses were coated by a carbon film (10−20 nm thickness) and examined by scanning electron microscopy (SEM) with a JSM 7000F (JEOL) microscope in backscatter electron imaging mode at 20 kV acceleration voltage; it confirmed that each specimen constitutes a single homogeneous amorphous phase. Cation contents were estimated using a LINK INCA (Oxford instruments) energy-dispersive X-ray (EDX) detector. Each sample composition was obtained as an average over 10 analyses from distinct fragments, with its respective oxygen content calculated to charge-balance the cations. The nominal and EDX-analyzed glass compositions agree well overall (see Table 1), with the largest losses observed for Na^+ and Ca^{2+}. The minor discrepancies between the nominal and analyzed compositions have no significant bearings on the interpretations or conclusions of the results reported herein. For convenience, we base the BG$n(p)$ sample nomenclature on the nominal glass compositions.

2.1.2. MBG Samples. The MBG86(3.4) and MBG58(4.3) specimens discussed herein are identical to those previously referred to as "S85" and "S58″, respectively, in our recent work,[24,25] to which we refer for additional details about characterizations and MBG textural properties. Here we only briefly recapitulate the most important information.

The MBG86(3.4) and MBG58(4.3) specimens of nominal compositions $10CaO−85SiO_2−5P_2O_5$ and $37CaO−58SiO_2−5P_2O_5$, respectively, were prepared by an EISA process employing the P123 triblock copolymer as structure-directing agent at 40 °C, as described by López-Noriega et al.[20] Tetraethyl orthosilicate (TEOS), triethyl phosphate (TEP), and $Ca(NO_3)_2\cdot4H_2O$ served as precursors for introducing each of the elements Si, P, and Ca, respectively. Each reaction product was calcined at 700 °C for 6 h to eliminate organic species and nitrate ions.

The cation compositions were determined by X-ray fluorescence (XRF) spectroscopy, by using a Philips PANanalytica AXIOS spectrometer (Philips Electronics NV) with X-rays generated at the Rh K_α line (λ = 0.614 Å). Except for some non-negligible losses of P, the XRF-analyzed compositions of $Ca_{0.10}Si_{0.84}P_{0.06}O_{1.93}$ [MBG86(3.4)] and $Ca_{0.36}Si_{0.55}P_{0.08}O_{1.66}$ [MBG58(4.3)] were close to the nominal ones; see Table 1 that also lists the corresponding oxide equivalents. Herein, we base our sample nomenclature on the analyzed compositions, which we believe give the most representative P contents of the samples. Further, the composition of the MBG86(3.4) specimen was independently analyzed by EDX coupled with both SEM (see Gunawidjaja et al.[25]) and transmission electron microscopy (TEM; see Mathew et al.[24]), giving the estimated compositions $Ca_{0.11}Si_{0.81}P_{0.08}O_{1.93}$ and $Ca_{0.10}Si_{0.86}P_{0.05}O_{1.95}$, respectively.

2.2. NMR Experiments. Unless stated otherwise, all ^{31}P and ^1H NMR experiments were performed with a Bruker Avance-III spectrometer at an external magnetic field of 9.4 T, which gives Larmor frequencies of −162.0 MHz for ^{31}P and −400.1 MHz for ^1H. Finely ground powders of each (M)BG$n(p)$ specimen were packed in 4 mm zirconia rotors, where full rotors were utilized throughout all NMR experimentation, except for that involving the ^{31}P spin-counting, which utilized samples restricted to 30% of the total rotor volume for minimizing rf inhomogeneity. No signal apodization was employed in the data processing. ^{31}P chemical shifts are quoted relative to 85% H_3PO_4.

$^1H\rightarrow^{31}P$ cross-polarization (CP) followed by a 90° pulse was employed throughout all MQC experimentation of the MBG samples to prepare longitudinal ^{31}P magnetization, owing to the very slow ^{31}P spin−lattice relaxation (T_1 > 150 s) coupled with their relatively low P contents. On the other hand, the Fe^{3+}-doped melt-prepared BGs are

associated with ^{31}P T_1 > 150 s and allowed for MQC excitation directly from magnetization at thermal equilibrium. The 2QC excitation and reconversion events were achieved by the symmetry-based $R20_2^9$ recoupling sequence operating at a ^{31}P nutation frequency of 54.0 kHz; see refs 38 and 39 for details about the $R20_2^9$ scheme and its implementation in a double-quantum filtering (2QF) protocol. For each τ_{exc}-value and sample, the 2QF *efficiency* was determined as the ratio between the integrated signal intensity after 2QF relative to that obtained from a "reference" single-pulse/CPMAS NMR spectrum obtained under otherwise identical experimental conditions.

The Supporting Information provides all detailed experimental conditions and data analysis for the 2QF and spin-counting ^{31}P NMR experiments.

3. RESULTS

3.1. ^{31}P MAS NMR Spectra. Figure 1 shows the ^{31}P MAS NMR spectra recorded directly by single pulses (black traces)
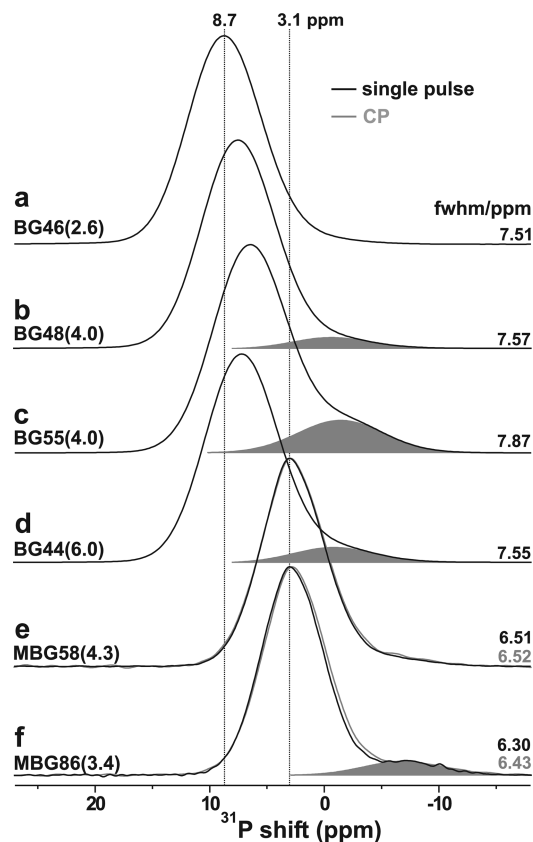
Figure 1. ^{31}P MAS NMR spectra recorded from the as-indicated samples by single pulses (a−f) and in (e, f) also by $^1H\rightarrow^{31}P$ CP. The full width at half-maximum height of each peak shape is specified at the right portion of each spectrum. All NMR spectra were recorded at 9.4 T; those of the BGs (a−d) were acquired at 7.0 kHz MAS with a 7 mm Bruker double resonance probehead by using τ_{90}^P = 4.1 μs and relaxation delays of 40 s. The data for the MBGs (e, f) are reproduced from Mathew et al.,[24] to which we refer for detailed experimental conditions. The shaded areas in (b−d, f) mark signal contributions from minor amounts of Q_P^1 moieties.

and for the MBGs also by $^1H\rightarrow^{31}P$ CPMAS (gray traces). As expected, all NMR spectra reveal P speciations dominated by orthophosphate ($^{31}PO_4^{3-}$) groups, whose NMR peak maxima span 3−9 ppm, depending on the relative Na^+/Ca^{2+} content of the BG sample.[11,27,28] The orthophosphates in the MBGs exhibit ^{31}P NMR peak maxima very similar to that of HAp

1879

dx.doi.org/10.1021/cm400487a | *Chem. Mater.* 2013, 25, 1877−1885

($\approx$3 ppm).[21,22,24,25] The observed Gaussian NMR peak-shape is associated with a full-width at half-maximum (fwhm) height in the range of 6.3−7.9 ppm and verifies orthophosphate ions in structurally disordered environments.[40]

Besides the orthophosphate groups, the P speciation comprises minor amounts of Q_P^1 moieties, where the superscript denotes the presence of one BO atom, implying either a P−O−**Si** or a P−O−**P** bonding scenario.[21] These ^{31}P NMR signals appear shifted by around −10 ppm from the Q_P^0 (i.e., orthophosphate) resonances, and spectral deconvolution is required to separate the two contributions: the MAS spectra in Figure 1 from BG48(4.0), BG44(6.0), BG55(4.0), and MBG86(3.4) revealed relative Q_P^1 populations of 7%, 10%, 20%, and 9% out of the total P speciation, respectively. The Q_P^1 moieties are attributed to P−O−Si bonds associated with the MBG surface; see Leonova et al.[21] and Fayon et al.[37] for further discussions on this assignment. In agreement with previous studies,[11,12,21] the BG46(2.6) (i.e., "45S5"[1]) and MBG58(4.3) samples manifest negligible Q_P^1 contributions, which for the melt-prepared BGs increases with the SiO_2 and P_2O_5 contents of the sample: see Figure 1a−d and Table 1.

3.2. Double-Quantum Filtering Experiments. As opposed to the "spin-counting" experimentation where all MQC orders are monitored, here the 2QC dynamics is selectively probed for increasing τ_{exc} under MAS conditions. The 2QC buildup rate, and thereby the τ_{exc}-value that optimizes the 2QF signal amplitude, relates directly to the set of largest dipolar coupling constants in the structure; the larger (shorter) the values of b_{jk} (r_{jk}), the faster the 2QC generation.

Figure 2a compares the ^{31}P MAS NMR spectra (black traces) from each (M)BG sample with the corresponding results (red traces) after application of 2QF that involves dipolar recoupling under MAS conditions.[38] While the structures of HAp, BG46(2.6), and MBG58(4.3) comprise essentially only the targeted orthophosphate (Q_P^0) species, those of BG48(4.0), BG55(4.0), BG44(6.0), and MBG86(3.4) required spectral deconvolutions to separate its NMR signal from that associated with the minor amounts of Q_P^1 species, by accounting both for the contributions from the central peak and the spinning sidebands appearing on its left and right flanks; see Figure 2b.
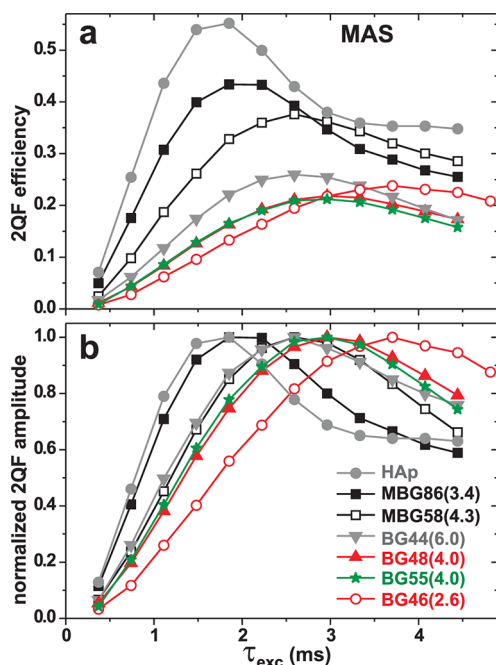
Figure 3 plots the [31]P 2QF efficiencies of the orthophosphate groups for increasing 2QC excitation intervals. For the melt-prepared BGn(p) (p = 2.6, 4.0, 6.0) specimens, the 2QC buildup rate of the orthophosphate groups increases proportionally with the P content of the glass. Essentially identical results are observed for the BG48(4.0) and BG55(4.0) specimens that only differ in their SiO_2 contents and network connectivities (see Table 1). The Ca-rich MBG58(4.3) structure that features a relatively fragmented silicate network (N_{BO} = 3.1) displays a 2QC growth similar to that of the melt-prepared BG44(6.0) glass of highest P content and N_{BO} = 2.5. On the contrary, the Ca-poor MBG86(3.4) sample, whose pore-wall constitutes nearly unmodified SiO_2 because its entire CaO reservoir is consumed by the orthophosphate species,[21−23] reveals a clearly accelerated 2QC generation; this verifies significantly shorter [31]P−[31]P internuclear distances (on the average) in the MBG86(3.4) structure relative to all other (M)BGs. Incidentally, its 2QC excitation rate is nearly as rapid as that from polycrystalline hydroxyapatite (HAp; $Ca_5(PO_4)_3OH$), where each crystallite may be considered a micrometer-sized CaP cluster. The 2QF data suggests comparable short/intermediate-range (<1 nm) [31]P−[31]P contacts in the MBG86(3.4) and HAp structures, whereas the orthophosphate ions are statistically (randomly)
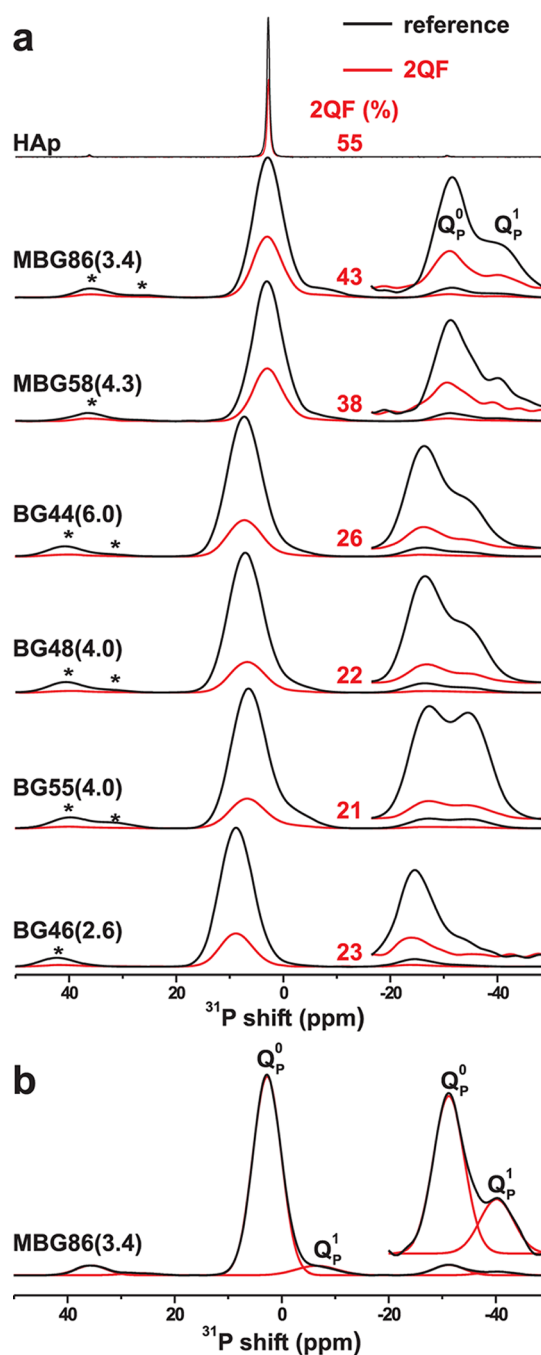
Figure 2. (a) 2QF ^{31}P MAS NMR spectra (red traces) acquired at 9.4 T and 5.4 kHz MAS from the as-indicated (M)BG specimens and shown together with "reference" spectra (black traces) obtained under otherwise identical experimental conditions, either directly by single pulses (for the BGs) or by [1]H→[31]P CP (for HAp and the MBGs). Asterisks mark spinning sidebands; the insets represent zooms over the spectral region involving the center peak and its nearest sidebands to the left and right. Each 2QF NMR spectrum was acquired at the τ_{exc}-value that optimized the 2QF efficiency (stated by red numbers) for the given sample (see Figure 3). (b) Spectral deconvolution into NMR signals from Q_P^0 and Q_P^1 groups of the MBG86(3.4) sample.

distributed in the BG specimens, thereby implying progressively longer [31]P−[31]P distances for decreasing P content.

We next consider the relative 2QF efficiencies in Figure 3a, which also correlate with our proposed P-clustering tendencies among the various (M)BG samples: the highest 2QF efficiency
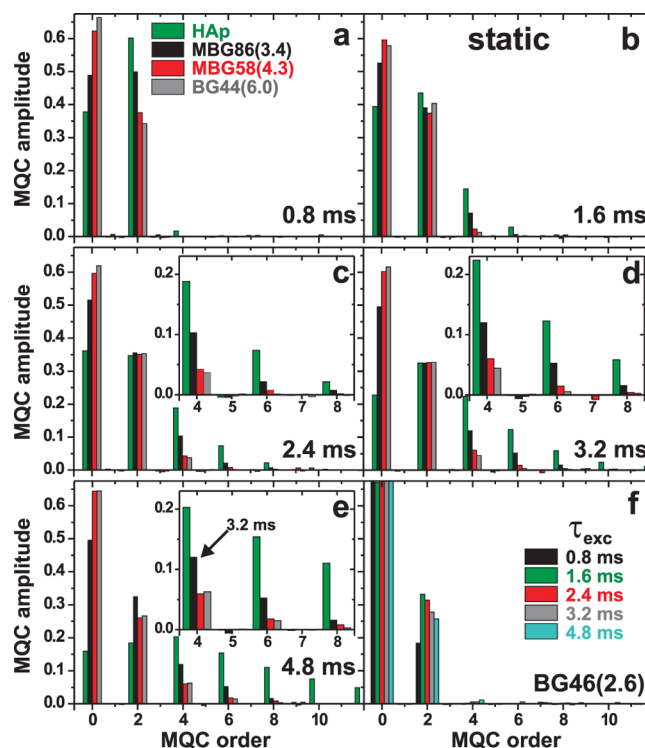
Figure 3. (a) 2QF efficiencies of the orthophosphate species in the as-indicated specimens, obtained under MAS conditions and plotted for increasing 2QC excitation intervals (τ_{exc}). The signal-buildup rate reflects the average $^{31}P-^{31}P$ distance. (b) Normalized 2QF amplitudes, emphasizing the distinct τ_{exc}-values where the 2QF amplitude is optimized. The data-uncertainty is within each symbol size.

Figure 4. (a−e) ^{31}P MQC NMR amplitudes plotted against the coherence order as generated by the technique of Baum et al.[34] from static (M)BG and HAp powders for increasing τ_{exc}-values of (a) 0.8 ms, (b) 1.6 ms, (c) 2.4 ms, (d) 3.2 ms, and (e) 4.8 ms (except for MBG86(3.4) in (e); τ_{exc} = 3.2 ms). The insets represent zooms around the MQC orders $4 \leq M \leq 8$. (f) Results from BG46(2.6) ["45S5" Bioglass] for the as-indicated τ_{exc}-values.

(55%) is obtained from crystalline HAp, whereas somewhat lower optimum values of 43% and 38% are observed from the MBG86(3.4) and MBG58(4.3) specimens, respectively. The BGs, on the other hand, reveal markedly lower efficiencies (22−26%). We attribute these trends as reflecting the various degrees of local PO_4^{3-}-aggregation among the structures: the relatively high 2QF losses associated with the BGs likely stem from their incorporation of a comparatively large fraction of "isolated" $^{31}PO_4^{3-}$ groups experiencing sufficiently large distances to their nearest ^{31}P neighbors that they are unable to participate in a 2QC state.

3.3. ^{31}P Spin-Counting Results. *3.3.1. Hydroxyapatite and MBG86(3.4).* The inferences about randomly distributed and clustered orthophosphate groups in BGs and MBGs, respectively, are corroborated by the spin-counting ^{31}P NMR results shown in Figure 4, where the excited MQC amplitudes from static powders are plotted against the coherence order for increasing τ_{exc} intervals. Figure S3 of the Supporting Information presents the same data as in Figure 4 but grouped so as to convey the coherence-growth from each (M)BG structure as τ_{exc} increases. Focusing on the *rate* of the MQC buildup, it declines according to HAp $\gg$ MBG86(3.4) $\gg$ MBG58(4.3)$\gtrsim$BG44(6.0) $\gg$ BG46(2.6). The HAp structure manifests significant 8QC excitation at τ_{exc} = 2.4 ms, whereas $\approx$22 mutually coupled orthophosphate groups are established at 4.8 ms (see the Supporting Information). All (M)BG samples display consistently slower high-order coherence growth, although weak 8QC excitation is evidenced already at τ_{exc} = 2.4 ms from MBG86(3.4), which exhibits significantly elevated MQC intensities relative to any other (M)BG specimen. Hence, the Si-rich MBG86(3.4) pore-walls display a clear phosphate-clustering tendency.

The slower MQC generation from MBG86(3.4) relative to crystalline HAp is attributed to (i) an overall looser phosphate-association due to the presence of water molecules within the amorphous CaP clusters,[24] and primarily (ii) their lower number of incorporated phosphate tetrahedra, where the data in Figure 4 provide a conservative lower bound of nine such groups and therefore a weaker coupled $^{31}P-^{31}P$ network. The latter follows because a 2Q Hamiltonian may only generate the highest *even* MQC order dictated by the spin system, meaning that if the real cluster-size is odd ($N_C = 2m + 1$; $m = 1, 2, 3,...$), the highest excitable coherence order is $2m$.[33−36] Another selection rule states that if the cluster comprises an integral multiple of four spins ($N_C = 4m$), then the extreme orders $M = \pm N_C$ cannot be excited.[35,41] Hence, as 8QC excitation was unambiguously established from the MBG86(3.4) sample, we conclude that the CaP clusters must comprise at least nine $^{31}PO_4^{3-}$ groups ($N_C \geq 9$).

3.3.2. Melt-Derived Glasses. High-order ($M > 4$) MQC excitation is readily attainable from *any* (M)BG sample, provided that sufficiently long τ_{exc}-values may be utilized to allow coherences to develop among $^{31}PO_4^{3-}$ groups spread over long distances of several nanometers. In practice, however, the high-order MQC excitation is for the present experimentation ultimately dictated by rf pulse errors and MQC relaxation, where the latter likely constitutes the major limiting factor. Our results from the HAp sample is one example, where only 22QC could be detected at our longest excitation interval (4.8 ms), despite that an astronomically larger number of orthophosphate groups are "clustering" in the micrometer-sized crystallites. Hence, our analysis is focused on semiquantitative comparisons between the MQC buildup *rates* among the samples, as well as monitoring the highest detectable coherence order at a given excitation interval.

Figure 5 compares the MQC profiles at two excitation intervals (2.4 and 4.8 ms) from MBG58(4.3) and three melt-prepared
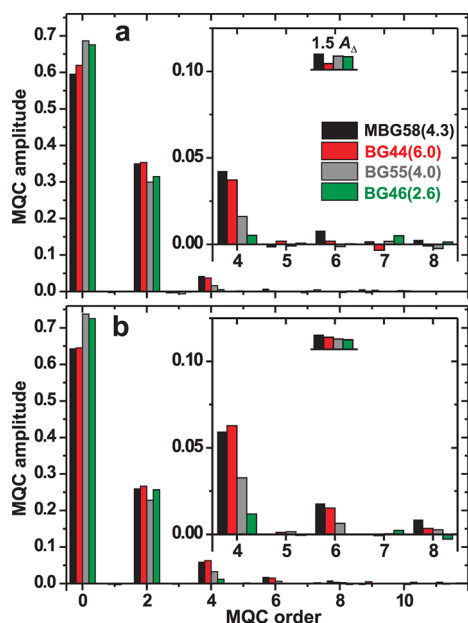
Figure 5. ^{31}P MQC amplitudes for increasing MQC order acquired with (a) $\tau_{exc} = 2.4$ ms and (b) $\tau_{exc} = 4.8$ ms from static powders. Results from the MBG58(4.3) specimen are compared with those of three melt-prepared glasses associated with different silicate-network connectivities and P_2O_5 contents: BG46(2.6), BG44(6.0), and BG55(4.0) (see Table 1). The latter sample comprises an essentially equal P_2O_5 content and a marginally lower N_{BO}-value of 2.9 relative to the EISA-generated MBG ($N_{BO} = 3.1$). The insets display zooms around the MQC orders $4 \leq M \leq 8$, also indicating the minimum signal intensity $1.5A_\Delta$ (see the Supporting Information) below which the observed MQC signal is considered insignificant. Note the enhanced MQC intensities observed from MBG58(4.3) relative to BG55(4.0) and its more rapid initial MQC excitation compared to BG44(6.0), which is attributed to a minor CaP clustering in the MBG pore-walls.

BGs, BG44(6.0), BG55(4.0), and BG46(2.6) that exhibit both variable P contents and widely spanning silicate-network connectivities of 2.5, 2.9, and 2.1, respectively (see Table 1). At the longest excitation interval (4.8 ms), the BG44(6.0), BG55(4.0), and BG46(2.6) structures only establish minor 6QC, 6QC, and 4QC intensities, respectively. The results of Figure 5 further underline the direct relationship between the MQC amplitudes observed from the melt-prepared BG and its amount of P (without any pronounced dependence on N_{BO}), as expected for a scenario of statistically dispersed orthophosphate ions, while the enhanced MQC developments stem solely from the gradually shortened ^{31}P–^{31}P distances as the P_2O_5 content increases. These findings also accord with computer modeling results that predict nonclustered orthophosphate groups in melt-prepared BGs featuring $\lesssim 6$ mol % P_2O_5, whereas P-richer structures manifest signatures of P aggregation.[29,30]

3.3.3. MBG58(4.3). While CaP clustering is established in the MBG86(3.4) pore-walls, the nature of the orthophosphate distribution in the MBG58(4.3) counterpart is less obvious. Further, Figures 4 and 5 (also see Figure S3 of the Supporting Information) reveal *initially* ($\tau_{exc} \leq 2.4$ ms) more rapid 4Q and 6Q excitation rates from the MBG58(4.3) sample relative to the P-richer BG44(6.0) specimen, whereas the latter provides somewhat faster MQC growth at larger τ_{exc}-values, such that

similar MQC profiles are observed from the two structures at the longest excitation interval of 4.8 ms. Note that the BG55(4.0) specimen features an essentially identical P content and a marginally lower N_{BO}-value relative to MBG58(4.3). Hence, when compared on essentially equal footings, it is clear from Figure 5 that the EISA-generated MBG structure displays markedly faster MQC excitation than its BG counterpart. This behavior suggests the presence of *small* Ca orthophosphate aggregates in the MBG58(4.3) pore-walls, thereby rationalizing why a relatively rapid initial MQC growth is observed, up to a point where the maximum excitable MQC order is reached within the aggregate, whereupon the generation of higher-order coherences is hampered by the longer ^{31}P–^{31}P *inter*cluster distances.

A different MQC excitation scenario applies for randomly spread PO_4^{3-} groups, such as in the BG44(6.0) structure, where the highest coherence order is mainly limited by the experimental conditions and relaxation, as discussed above. The same trend is observed in Figure 3: as the rate and efficiency of the 2QC generation emphasize the strongest couplings within the spin topology (i.e., the short-range structure), small CaP clusters, such as those of the MBG58(4.3) pore-walls, may provide markedly more efficient 2QC excitation than a structure featuring statistically dispersed P species [such as those of BG44(6.0)], even if the latter also exhibits sufficiently many short ^{31}P–^{31}P distances to provide an essentially equal *high-order* MQC profile over long excitation intervals.

4. DISCUSSION

4.1. Quantitating the Nature of the Orthophosphate Distributions. *4.1.1. Methodology and General Concerns.* To gain more quantitative insight into the orthophosphate distribution in each (M)BG structure, the ^{31}P 2QF NMR results of Figure 3a were analyzed in the regime of *short* 2QC excitation intervals. As discussed in refs 42–44, the 2QC buildup $[f_{2QF}(\tau_{exc})]$ then approximatively displays a parabolic dependence on the product between τ_{exc} and a scaled effective dipolar coupling constant (κb_{eff}^{exp}),

$$f_{2QF}(\tau_{exc}) \approx \frac{6}{5}(\kappa b_{eff}^{exp}\tau_{exc})^2 , \quad (1)$$

where $\kappa = 0.1743$ is a scaling factor associated with the $R20_2^9$ pulse scheme.[38,39] The effective ^{31}P dipolar coupling constant of the structure is proportional to the van Vleck second moment (M_2)[45] and relates to those of the individual pairs as

$$b_{eff}^2 = \sum_{j<k}^{\text{all pairs}} b_{jk}^2 . \quad (2)$$

Assessments of the relative experimental b_{eff}^{exp} values, and hence the corresponding "effective" ^{31}P–^{31}P internuclear distances, $r_{eff}^{exp} \sim (b_{eff}^{exp})^{-1/3}$, may be made by fitting the experimental 2QF efficiencies to eq 1 and comparing the results with calculated parameters obtained from different phosphate distribution models. To minimize systematic errors from imperfect dipolar recoupling and thereby optimizing the reliability of each experimental data point, it was recorded at completed $R20_2^9$ cycles. Unfortunately, this implies a relatively coarse sampling of the $f_{2QF}(\tau_{exc})$ curves, particularly for those of HAp and MBG86(3.4) that exhibit the most rapid 2QC dynamics. To ensure strict validity of eq 1, the fitting involved either solely the first 2QF efficiency-value or the first two data-points.

The best-fit results are plotted in Figure S4 of the Supporting Information, and Table 2 lists the corresponding b_{eff}^{exp} parameters.

Table 2. Effective $^{31}PO_4$–$^{31}PO_4$ Contacts Derived from 2QF NMR Data[a]

sample	$-b_{eff}^{exp}/2\pi$ (Hz)[b]	$-b_{eff}^{calc}[R]/2\pi$ (Hz)[c]	$-b_{eff}^{calc}[U]/2\pi$ (Hz)[c]	$-b_{eff}^{calc}[C]/2\pi$ (Hz)[d]	r_{eff}^{exp} (pm)[e]
HAp	609 (609)	665[f]			319 (310)[g]
MBG86(3.4)	509 (495)	193; 216	86	350; 385	338
MBG58(4.3)	353 (361)	233; 259	122	356; 390	382
BG44(6.0)	296 (284)	283; 313	174	370; 403	405
BG48(4.0)	243 (236)	229; 255	118	355; 389	433
BG55(4.0)	240 (235)	227; 252	116	354; 389	435
BG46(2.6)	200 (189)	184; 205	79	349; 384	462

[a]Best-fit parameters ($b_{eff}^{exp} \pm 8$ Hz; $r_{eff}^{exp} \pm 3$ pm) obtained from the data in Figure 3a. [b]b_{eff}^{exp} as obtained by fitting solely the first 2QF data-point to eq 1, with the corresponding result of also including the second 2QF value shown within parentheses. [c]Calculated effective coupling constants, assuming that the orthophosphate species are randomly ($b_{eff}^{calc}[R]$) or uniformly ($b_{eff}^{calc}[U]$) distributed. The left and right values were obtained by only allowing P–P distances longer than 410 and 380 pm, respectively. [d]Calculated results by assuming uniformly distributed clusters of five phosphate groups, extracted from the structures of HAp[46] (left value) and β-Ca$_3$(PO$_4$)$_2$[47] (right value). [e]NMR-derived effective P–P interatomic distances calculated from $r_{eff}^{exp} = (-4\pi b_{eff}^{exp}/[\mu_0 \hbar \gamma_P^2])^{-1/3}$, where γ_P is the magnetogyric ratio of ^{31}P. [f]Reference value calculated from the crystal structure by using eq 2. [g]Results obtained by either NMR or XRD, with the latter value shown within parentheses.

Given the potentially compromised accuracy stemming from the very low number of experimental data-points, it is gratifying that the two fits accord very well (see Table 2); we henceforth only discuss the first entries in the second column of Table 2. For HAp, the NMR-derived effective dipolar coupling constant $|b_{eff}^{exp}/2\pi| = 609$ Hz shows acceptable agreement with the value of 665 Hz calculated from eq 2 by using the XRD-derived atomic coordinates of ref 46. The estimates from NMR and XRD accord within 9%, which translates into <3% discrepancy between their respective effective interatomic distances (r_{eff}) in Table 2. Note that r_{eff} has no direct physical interpretation other than providing a conservative lower bound of the shortest ^{31}P–^{31}P internuclear distance present in the structure. For instance, the closest PO$_4^{3-}$–PO$_4^{3-}$ contact is 411 pm in the crystal structure of HAp,[46] whereas the r_{eff}-value derived from eq 2 amounts only to 310 pm. Hence, "large" values, $r_{eff}^{exp} > 400$ pm in Table 2, imply structures associated with long P–P separations ($\gtrsim$500 pm), which may be contrasted with the shortest PO$_4^{3-}$–PO$_4^{3-}$ contacts in crystalline Ca-based orthophosphates that span about 380–420 pm.[46−48]

To deepen the understanding of the data in Table 2, the NMR-derived effective dipolar coupling constants were compared with calculated counterparts (b_{eff}^{calc}) representative for uniform (U), random (R), or clustered (C) orthophosphate dispersions. The U/R results were obtained as averages over 20 configurations, each comprising 27 000 P atoms distributed in a cubic box, whose length was adjusted to match the experimentally determined density (Table 1) of each sample. Unphysical P–P contacts were avoided for the random distributions by redistributing the P atoms until the distance in any pair exceeded an assumed minimum threshold value (d_{min}) of either 410 pm or 380 pm, corresponding to the shortest PO$_4^{3-}$–PO$_4^{3-}$ distances observed in the (prototypic) crystal structures of HAp[46] and β-Ca$_3$(PO$_4$)$_2$,[47] respectively (while those in β-NaCaPO$_4$ amount

to 422 pm[48]). The "clustered" scenario was obtained by uniformly distributing (as in the "U" model) replicas of selected aggregates of five nearest-neighboring phosphate ions present in each of the HAp and β-Ca$_3$(PO$_4$)$_2$ structures: the $b_{eff}^{calc}[C]$ values in Table 2 were obtained as averages over the b_{eff}-values resulting from several calculations, each based on a unique local motif in the crystal structure.

As expected, we may safely *exclude uniformly* (homogeneously) dispersed orthophosphate species in any (M)BG structure from the markedly lower predicted $b_{eff}^{calc}[U]$ values relative to the experimental results (see Table 2).

4.1.2. Melt-Derived Glass Structures. We first consider the phosphate dispersion in the melt-prepared BG specimens, where the effective coupling constants derived from a statistical distribution provide semiquantitative agreement with the experiments (see Table 2). Figure 6a,b illustrates the suggested phosphate
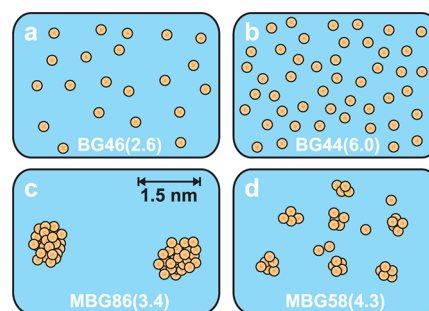
Figure 6. Schematic illustrations of the distributions of orthophosphate groups (yellow circles) encountered across the dominating silicate matrix (blue) in melt-prepared BGs incorporating (a) low and (b) high amounts of P, representative for the BG46(2.6) and BG44(6.0) compositions, respectively. Calcium orthophosphate clusters observed in the pore-walls of (c) MBG86(3.4) and (d) MBG58(4.3).

dispersion in melt-prepared BG structures (at least for P$_2$O$_5$ contents $\lesssim$ 6 mol %).

The $b_{eff}^{calc}[R]$ values in Table 2 depend slightly on the choice of d_{min}. This illustrates the well-known feature that randomly distributed species inherently display some minor degree of "clustering", for instance manifested by the formation of constellations of stars in the night sky. Hence, it is difficult to distinguish a random distribution from a "very weakly clustered" scenario if NMR results are only available from a sole glass composition. On the basis of the unambiguous excitation of 4QC by ^{31}P NMR spin-counting, Fayon et al.[37] argued for the presence of small aggregates of five to six phosphate groups in a glass of similar composition to our BG46(2.6) specimen. Up to the longest MQC excitation interval of 4.8 ms employed herein, our experimental NMR data are fully consistent with those of ref 37, as are the predictions of their stated "cluster sizes" emerging from a Gaussian fit of the MQC amplitudes by following the procedure of refs 34−36. However, as this analysis has been criticized,[49] particularly for making inferences from data involving only low MQC orders (here $M \leq 4$), we follow the recommendations of Lacelle et al.[49] and merely draw conservative conclusions about *lower-limit* estimates of the number of correlated phosphate tetrahedra, as dictated by the highest MQC order *observed*.

Noteworthy, all spin-counting NMR data reported herein reveal a monotonically growing number of $^{31}PO_4^{3-}$ groups participating to the high-order MQ excitation for an increase of either the P content of the BG or the τ_{exc}-value of the NMR

experiment: this is naturally rationalized by MQC excitation among phosphate groups that exhibit gradually shortened $^{31}P-^{31}P$ distances as the P_2O_5 content of the sample increases. These observations are in stark contrast with the predictions from a pronounced P clustering scenario: by instead assuming BGs comprising uniformly distributed clusters of five PO_4^{3-} groups in their structures, the resulting $|b_{eff}^{calc}[C]|$ values are overall significantly higher than those observed experimentally in Table 2. Most important, however, is that such a clustering model fails to reproduce even the gross qualitative experimental trends of growing $|b_{eff}^{exp}|$ values for increasing P_2O_5 content of the glass. Moreover, if instead assuming randomly distributed clusters, all calculated effective coupling constants increase slightly relative to the uniform cluster dispersion, but their relative magnitudes remain largely intact. Altogether, it appears difficult to reconcile our experimental data from the BGs by any pronounced orthophosphate clustering (other than that naturally commensurate with a nonuniform P dispersion inherent to the statistical distribution).

4.1.3. MBG Structures. Contrary to the situation in melt-prepared BGs, the CaP clusters in the MBG pore-walls represent groups of $Ca_3(PO_4)_2$ motifs that, except for their smaller size and inherently disordered nature, have direct counterparts in crystalline orthophosphate-based structures. Hence, they are expected to feature marginally lower (higher) values of b_{eff} (r_{eff}) relative to their crystalline mother-structures; this criterion is indeed met by MBG86(3.4), whose value of r_{eff}^{exp} = 338 pm is only $\approx$20 pm longer than that observed from HAp (see Table 2). Noteworthy, the model of statistically distributed orthophosphate groups predicts a b_{eff}^{calc}-value less than half of its experimental counterpart.

Our spin-counting experiments (section 3.3.1) provided a lower bound of nine phosphate groups in the CaP clusters. The actual numbers are likely larger. Indeed, aggregates of 20−40 phosphate species derived from the HAp and β-$Ca_3(PO_4)_2$ structures provide $|b_{eff}^{calc}[C]/2\pi|$ values around the experimental result of $|b_{eff}^{exp}/2\pi| \approx$500 Hz. Such CaP clusters are associated with diameters in the range 1.5−2 nm (see Figure 6c), which may be contrasted with the pore-wall thickness $\approx$3.5 nm of MBG86(3.4).[21] Hence, our previously suggested dual-phase pore-wall picture is here unambiguously established for the case of MBG86(3.4); see Figure 8 of Leonova et al.[21] for a schematic illustration.

Our inferences of a minor CaP clustering in the MBG58(4.3) pore-walls are also corroborated further by the following observations: (i) A scenario of statistically dispersed phosphate groups may be excluded on the basis of its significantly lower $|b_{eff}^{calc}[R]|$ predictions relative to that of $|b_{eff}^{exp}/2\pi| \approx$350 Hz, whereas now (ii) clusters of five phosphate ions accord much better with experiments (see Table 2). Most likely, the MBG58(4.3) pore-walls pore-walls exhibit a large number of randomly dispersed small CaP clusters, as illustrated in Figure 6d: the cluster-size distribution is shifted toward relatively few (four to six) groups that feature some sufficiently short intercluster distances to allow for excitation of MQC orders up to $\approx$8 in our spin-counting experiments (Figures 4 and 5).

4.2. The Driving Forces for Phosphate Clustering in MBGs. The phosphate ions are randomly distributed in melt-prepared BGs, where they naturally occupy interstitial positions around the highly fragmented silicate network. Further, as inferred from the monotonic MQC excitation trends for increasing P content of the BG, there is no obvious dependency of the orthophosphate distribution on the silicate network connectivity

for fragmented glass structures (see Figures 3 and 5). However, for highly polymerized networks, such as those of MBG86(3.4) that features $N_{BO} \approx 4$, the insufficient space to accommodate the PO_4^{3-} species induces inhomogeneities in the pore-walls that exhibit separate SiO_2 and $CaO-P_2O_5$ domains. We conclude that a pronounced CaP aggregation is primarily a feature of Ca-depleted networks of silica-rich MBGs [i.e., MBG86(3.4), as opposed to MBG58(4.3)]. The nanometer-scale segregation of the dense MBG86(3.4) pore-walls is analogous to the macroscopic phase-separation/crystallization tendencies into silicate- and phosphate-rich domains observed for melt-prepared BG compositions featuring high amounts of P and relatively low modifier contents.[27,50,51]

Yet, the nature of the P dispersion is also dictated by the preparation method of the sample, with EISA/sol−gel-generated structures exhibiting stronger P-aggregation relative to its melt-quench counterparts for otherwise comparable glass compositions, i.e., MBG58(4.3) vs BG55(4.0). This may be rationalized as stemming from distinct kinetics of the hydrolysis and condensation stages of the TEP and TEOS precursors used to introduce P and Si, respectively, where the alkoxide hydrolysis constitutes the rate-limiting step of the process under acidic conditions. The hydrolysis rate of TEOS is faster than that of TEP, as it strongly correlates with the electronegativity of the central atom; the higher the electronegativity, the slower the hydrolysis. Consequently, the different hydrolysis kinetics between TEOS and TEP may provide significant heterogeneities in the resulting structure. Because the TEOS hydrolysis/condensation processes are initiated before those of TEP, a covalent network mainly involving silica is formed for Si-rich compositions. The P incorporation is slightly delayed, where Ca^{2+} and PO_4^{3-} ions partially aggregate among themselves to form CaP clusters.

5. CONCLUSIONS

Our experimental data furnish the following *variable* structural role of the orthophosphate ions in (M)BGs, which depends foremost on the SiO_2 content of the sample and second on its preparation method: in relatively fragmented melt-prepared glass structures featuring low/medium P contents ($\lesssim$6 mol % P_2O_5), the phosphate anions are randomly distributed, naturally occupying interstitial positions together with the Na^+/Ca^{2+} cations. This P-dispersion scenario remains, provided that the silicate network is sufficiently fragmented to readily accommodate the phosphate groups.

However, for very dense 3D networks ($N_{BO} \approx 4$), such as that of MBG86(3.4), there is insufficient space for incorporating significant amounts of PO_4^{3-} groups, which drives a nanometer-scale separation of the MBG pore-walls into two amorphous components, i.e., SiO_2 and CaP. Our experimental data directly establish a lower bound of nine PO_4^{3-} groups present in the clusters of the MBG86(3.4) pore-walls, while further analyses predict approximate cluster sizes of 20−40 groups that exhibit diameters around 1.5−2 nm. The surface-association of the CaP clusters coupled with the high surface-area provides an excellent in vitro bioactivity of MBG86(3.4),[21−24,26] despite its very Si-rich composition that is well outside the range where melt-derived glasses exhibit physiological responses.[1,3,6−10]

The pore-wall segregation is markedly less pronounced in the Ca-richer MBG58(4.3) sample due to its more open silicate network. Yet, this structure provides faster initial MQC developments relative to melt-prepared BGs of equal or even higher P_2O_5 contents. The MBG58(4.3) specimen most likely involves a *range* of *small* CaP clusters that typically comprise four to six groups. Hence, relative to melt-prepared BGs, the elevated

HCA formation-rates observed in vitro from modifier-rich MBGs—such as MBG58(4.3), or sol−gel-derived BGs (vide infra)—stem primarily from their significantly higher surface area accompanying the porous texture.

In summary, we have demonstrated the power of combining NMR spin-counting and 2QF experiments for probing the orthophosphate distribution in silicate glasses. This approach may provide semiquantitative estimates of orthophosphate cluster sizes and P−P interatomic distances and may be exploited to study the P-dispersion in other biomaterials, as well as for monitoring the initial Ca phosphate-aggregation processes at the surfaces of (P-free) biomaterials in vitro.

■ ASSOCIATED CONTENT

Ⓢ Supporting Information

Further information about NMR experiments, including additional experimental results, is available free of charge via the Internet at http://pubs.acs.org.

■ AUTHOR INFORMATION

Corresponding Author
*E-mail: mattias.eden@mmk.su.se; fax: +46 8 152187; phone: +46 8 162375.

Notes
The authors declare no competing financial interest.

■ ACKNOWLEDGMENTS

■ REFERENCES

(1) Hench, L. L. *J. Am. Ceram. Soc.* **1991**, *74*, 1487.
(2) Hench, L. L.; Polak, J. M. *Science* **2002**, *295*, 1014.
(3) Jones, J. R. *Acta Biomater.* **2013**, *9*, 4457.
(4) Arcos, D.; Vallet-Regi, M. *Acta Biomater.* **2010**, *6*, 2874.
(5) Ohtsuki, C.; Kokubo, T.; Yamamuro, T. *J. Non-Cryst. Solids* **1992**, *143*, 84.
(6) Lebecq, I.; Désanglois, F.; Leriche, A.; Follet-Houttemane, C. *J. Biomed. Mater. Res. A* **2007**, *83*, 156.
(7) Strnad, Z. *Biomaterials* **1992**, *13*, 317.
(8) O'Donnell, M. D.; Watts, S. J.; Hill, R. G.; Law, R. V. *J. Mater. Sci. Mater. Med* **2009**, *20*, 1611.
(9) Hill, R. G.; Brauer, D. S. *J. Non-Cryst. Solids* **2011**, *357*, 3884.
(10) Edén, M. *J. Non-Cryst. Solids* **2011**, *357*, 1595.
(11) FitzGerald, V.; Pickup, D. M.; Greenspan, D.; Sarkar, G.; Fitzgerald, J. J.; Wetherall, K. M.; Moss, R. M.; Jones, J. R.; Newport, R. J. *Adv. Funct. Mater.* **2007**, *17*, 3746.
(12) Pedone, A.; Charpentier, T.; Malavasi, G.; Menziani, M. C. *Chem. Mater.* **2010**, *22*, 5644.
(13) Brinker, C. J.; Lu, Y. F.; Sellinger, A.; Fan, H. Y. *Adv. Mater.* **1999**, *11*, 579.
(14) Ebisawa, Y.; Kokubo, T.; Ohura, K.; Yamamuro, T. *J. Mater. Sci. Mater. Med.* **1990**, *1*, 239.
(15) Skipper, L. J.; Sowrey, F. E.; Rashid, R.; Newport, R. J.; Lin, Z.; Smith, M. E. *Phys. Chem. Glasses* **2005**, *46*, 372.
(16) Lin, K. S. K.; Tseng, Y. H.; Mou, Y.; Hsu, Y. C.; Yang, C. M.; Chan, J. C. C. *Chem. Mater.* **2005**, *17*, 4493.
(17) Lin, S.; Ionescu, C.; Pike, K. J.; Smith, M. E.; Jones, J. R. *J. Mater. Chem.* **2009**, *19*, 1276.
(18) Yan, X. X.; Yu, C. Z.; Zhou, X. F.; Tang, J. W.; Zhao, D. Y. *Angew. Chem., Int. Ed.* **2004**, *43*, 5980.
(19) Yan, X. X.; Huang, X. H.; Yu, C. Z.; Deng, H. X.; Wang, Y.; Zhang, Z. D.; Qiao, S. Z.; Lu, G. Q.; Zhao, D. Y. *Biomaterials* **2006**, *27*, 3396.
(20) López-Noriega, A.; Arcos, D.; Izquierdo-Barba, I.; Sakamoto, Y.; Terasaki, O.; Vallet-Regí, M. *Chem. Mater.* **2006**, *18*, 3137.
(21) Leonova, E.; Izquierdo-Barba, I.; Arcos, D.; Lopez-Noriega, A.; Hedin, N.; Vallet-Regí, M.; Edén, M. *J. Phys. Chem. C* **2008**, *112*, 5552.
(22) Gunawidjaja, P. N.; Lo, A. Y. H.; Izquierdo-Barba, I.; García, A.; Arcos, D.; Stevensson, B.; Grins, J.; Vallet-Regí, M.; Edén, M. *J. Phys. Chem. C* **2010**, *114*, 19345.
(23) Gunawidjaja, P. N.; Mathew, R.; Lo, A. Y. H.; Izquierdo-Barba, I.; García, A.; Arcos, D.; Vallet-Regí, M.; Edén, M. *Philos. Trans. R. Soc. A* **2012**, *370*, 1376.
(24) Mathew, R.; Gunawidjaja, P. N.; Izquierdo-Barba, I.; Jansson, K.; García, A.; Arcos, D.; Vallet-Regí, M.; Edén, M. *J. Phys. Chem. C* **2011**, *115*, 20572.
(25) Gunawidjaja, P. N.; Izquierdo-Barba, I.; Mathew, R.; Jansson, K.; García, A.; Grins, J.; Arcos, D.; Vallet-Regí, M.; Edén, M. *J. Mater. Chem.* **2012**, *22*, 7214.
(26) García, A.; Cicuéndez, M.; Izquierdo-Barba, I.; Arcos, D.; Vallet-Regí, M. *Chem. Mater.* **2009**, *21*, 5474.
(27) Lockyer, M. W. G.; Holland, D.; Dupree, R. *J. Non-Cryst. Solids* **1995**, *188*, 207.
(28) Elgayar, I.; Aliev, A. E.; Boccaccini, A. R.; Hill, R. G. *J. Non-Cryst. Solids* **2005**, *351*, 173.
(29) Tilocca, A.; Cormack, A. N. *J. Phys. Chem. B* **2007**, *111*, 14256.
(30) Tilocca, A. *Proc. R. Soc. A* **2009**, *465*, 1003.
(31) Vallet-Regí, M.; Salinas, A. J.; Ramirez-Castellanos, J.; Gonzalez-Calbet, J. M. *Chem. Mater.* **2005**, *17*, 1874.
(32) Aguiar, H.; Solla, E. L.; Serra, J.; González, P.; León, B.; Almeida, N.; Cachinho, S.; Davim, E. J. C.; Correia, R.; Oliveira, J. M.; Fernandes, M. H. V. *J. Non-Cryst. Solids* **2008**, *354*, 4075.
(33) Yen, Y. S.; Pines, A. *J. Chem. Phys.* **1983**, *78*, 3579.
(34) Baum, J.; Munowitz, M.; Garroway, A. N.; Pines, A. *J. Chem. Phys.* **1985**, *83*, 2015.
(35) Munowitz, M.; Pines, A.; Mehring, M. *J. Chem. Phys.* **1987**, *86*, 3172.
(36) Hughes, C. E. *Prog. Nucl. Magn. Reson. Spectrosc.* **2004**, *45*, 301.
(37) Fayon, F.; Duée, C.; Poumeyrol, T.; Allix, M.; Massiot, D. *J. Phys. Chem. C* **2013**, *117*, 2283.
(38) Marin-Montesinos, I.; Brouwer, D. H.; Antonioli, G.; Lai, W. C.; Brinkmann, A.; Levitt, M. H. *J. Magn. Reson.* **2005**, *177*, 307.
(39) Pileio, G.; Concistre, M.; McLean, N.; Gansmulller, A.; Brown, R. C. D.; Levitt, M. H. *J. Magn. Reson.* **2007**, *186*, 65.
(40) MacKenzie, K. J. D.; Smith, M. E. *Multinuclear solid-state NMR of inorganic materials*; Pergamon Press: Amsterdam, 2002.
(41) Tycko, R. *J. Magn. Reson.* **1999**, *139*, 302.
(42) Saalwachter, K.; Ziegler, P.; Spyckerelle, O.; Haidar, B.; Vidal, A.; Sommer, J. U. *J. Chem. Phys.* **2003**, *119*, 3468.
(43) Saalwachter, K.; Lange, F.; Matyjaszewski, K.; Huang, C. F.; Graf, R. *J. Magn. Reson.* **2011**, *212*, 204.
(44) Tseng, Y. H.; Tsai, Y. L.; Tsai, T. W. T.; Lin, C. P.; Huang, S. H.; Mou, C. Y.; Chan, J. C. C. *Solid State Nucl. Magn. Reson.* **2007**, *31*, 55.
(45) van Vleck, J. H. *Phys. Rev.* **1948**, *74*, 1168.
(46) Sudarsanan, K.; Young, R. A. *Acta Crystallogr., Sect. B: Struct. Crystallogr. Cryst. Chem.* **1969**, *25*, 1534.
(47) Yashima, M.; Sakai, A.; Kamiyama, T.; Hoshikawa, A. *J. Solid State Chem.* **2003**, *175*, 272.
(48) Ben Amara, M.; Vlasse, M.; Leflem, G.; Hagenmuller, P. *Acta Crystallogr.* **1983**, *39*, 1483.
(49) Lacelle, S.; Hwang, S. J.; Gerstein, B. C. *J. Chem. Phys.* **1993**, *99*, 8407.
(50) Chen, X. F.; Hench, L. L.; Greenspan, D.; Zhong, J. P.; Zhang, X. K. *Ceram. Int.* **1998**, *24*, 401.
(51) Linati, L.; Lusvardi, G.; Malavasi, G.; Menabue, L.; Menziani, M. C.; Mustarelli, P.; Segre, U. *J. Phys. Chem. B* **2005**, *109*, 4989.